ACS MATERIALS LETTERS

www.acsmaterialsletters.org

LETTER

Strain-Directed Layer-By-Layer Epitaxy Toward van der Waals Homo- and Heterostructures

Yi Wan, Jing-Kai Huang, Chih-Piao Chuu, Wei-Ting Hsu, Chien-Ju Lee, Areej Aljarb, Chun-Wei Huang, Ming-Hui Chiu, Hao-Ling Tang, Ci Lin, Xuechun Zhang, Ching-Ming Wei, Sean Li, Wen-Hao Chang, Lain-Jong Li,* and Vincent Tung*

Cite This: *ACS Materials Lett.* 2021, 3, 442−453

Read Online

ACCESS | Metrics & More | Article Recommendations | Supporting Information

ABSTRACT: **Transition-metal dichalcogenide (TMDC) homo- and heterostacks hold tantalizing prospects for being integrated as active components in future van der Waals (vdW) electronics and optoelectronics. However, most TMDC homo- and heterostacks are created by onerous mechanical exfoliation, followed by a mixing-and-matching process. While versatile enough for pilot demonstrations, these strategies are clearly not scalable for practical technologies and widespread implementations. Here, we report a two-step epitaxy strategy that promotes the growth of second-layer TMDCs on the basal plane of the first TMDCs epilayer. The first-layer TMDCs are grown on substrates where the tensile strength can be tuned by the control of chemical environments. The succeeding epilayers then prefer to grow layer-by-layer on the highly tensile-strained first layers. The result is the growth of high-density TMDC homo (WSe_2) bilayers and hetero (WSe_2−MoS_2) bilayers with an exceedingly high yield (>99% bilayers) and uniformity. A density functional theory simulation further sheds light on how strain engineering shifts the subsequent layer growth preference. Second-harmonic generation and high-angle annular dark-field scanning transmission electron microscopy collectively attest to the AB and AA′ stacking between the TMDC epi- and overlayers. The proposed strategy could be a versatile platform for synthesizing diverse arrays of vdW homo- and heterostacks, thus providing prospects for realizing large-scale and layer-controllable two-dimensional electronics.**

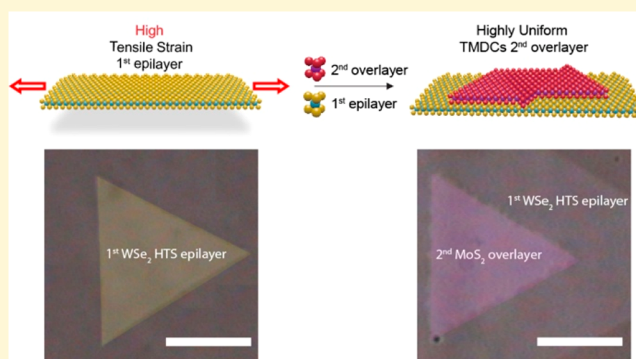

Two-dimensional (2D) van der Waals (vdW) structures embody a unique class of acritical lattices in which material properties can be manipulated via varying the composition, stacking orders, and relative orientation across the atomically thin junctions. Building such artificial vdW junctions is made possible by disassembling bulk crystals into 2D monolayers and reassembling them into bilayer artificial lattices, yielding access to a plethora of exciting physics.[1,2] The variety of artificial homo- and heterostructures can be further extended when combined with the recent rediscoveries of transition-metal dichalcogenides (TMDCs), therefore providing a route to previously unachievable semiconductor junctions, superlattices, and light−matter interactions.[3] Notable discoveries include but are not limited to the advent of atomically thin p−n junctions for the ultimate functional unit for nanoscale electronic and optoelectronic devices,[4−6] exceedingly high density of states that induce exceptionally high drive currents in the ballistic limit,[7,8] enhanced light absorption with a wider spectral response in UV and near-infrared (NIR) regions,[9,10] and prominent mechanical durability implemented in flexible devices.[11] Despite the immense interest and continuing experimental success by directly mixing and matching monolayer flakes of different materials, a widespread implementation of vdW homo- and heterostacks has yet to occur. This is primarily due to the difficulty of identifying a general, scalable, and reliable epitaxy mechanism that drives the direct growth of vdW homo- and heterostacks with control

Received: November 30, 2020
Accepted: February 22, 2021
Published: March 25, 2021

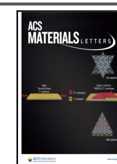

Downloaded via 147.8.230.77 on October 12, 2022 at 03:38:31 (UTC).
See https://pubs.acs.org/sharingguidelines for options on how to legitimately share published articles.

© 2021 The Authors. Published by American Chemical Society

https://doi.org/10.1021/acsmaterialslett.0c00554
ACS Materials Lett. 2021, 3, 442−453

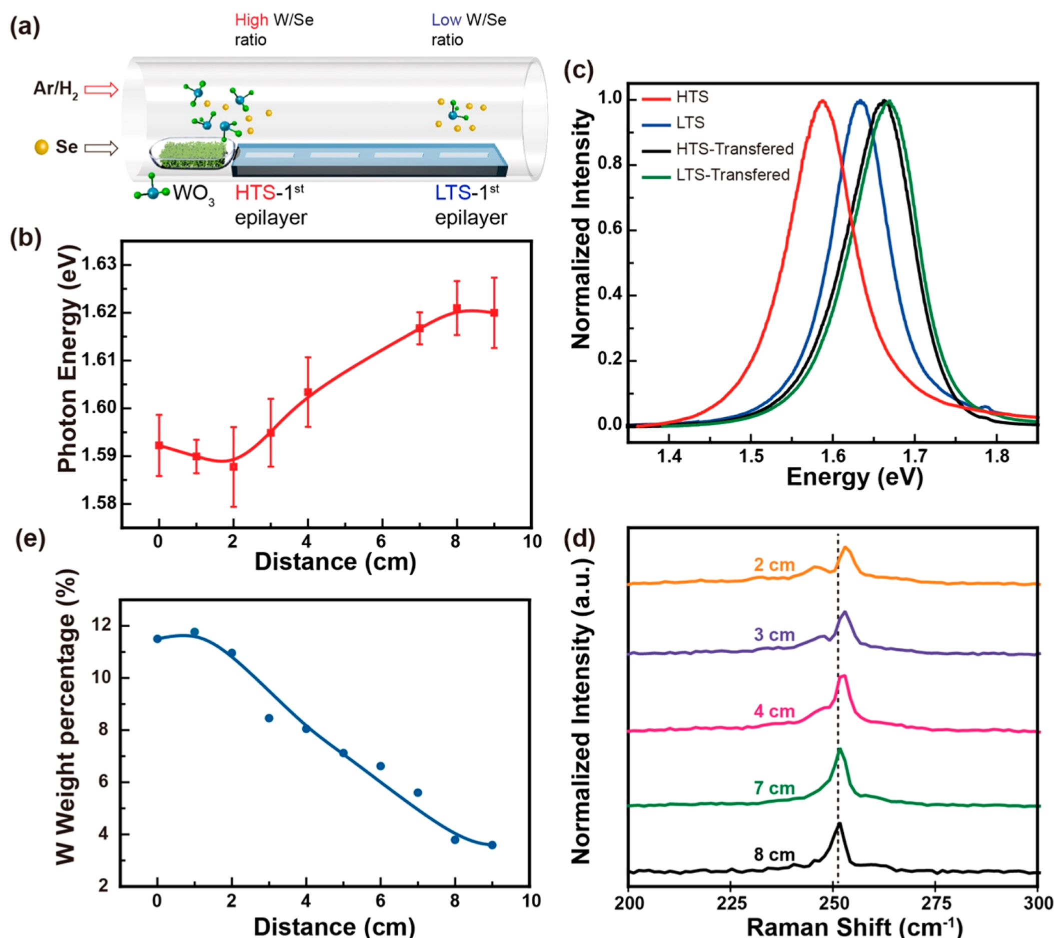

Figure 1. Strain engineering of the first WSe_2 epilayers. (a) Schematic illustration shows a representative CVD epitaxy growth of the first WSe_2 epilayers. (b) Photon energy distribution of the first WSe_2 epilayers collected at different distances away from the WO_3 source. Error bars are included to provide a standard deviation of photon energy. Data were collected from over 50 samples. (c) PL spectra of HTS and LTS first WSe_2 epilayers grown on sapphire substrates before and after transferring at room temperature. (d) Raman spectra of the as-grown first WSe_2 epilayers collected at different distances from away the WO_3 source. (e) The concentration distribution of W (blue) as a function of different distances away from the WO_3 source. The weight percentage of W with respect to detected elements (Al, O, and W) based on EDX data.

over bilayer coverage and content in tandem with the preservation of crystal qualities.

The general epitaxy growth in chemical vapor deposition (CVD) usually involves the vaporization of precursors, nucleation of TMDC seeds, and the stitching of individual seeding flakes. In this light, the vertical growth of homo- and heterostructures shall, in principle, be accomplished through the successive growth of a second material on the basal plane of a first layer. Currently, significant efforts have been reported to grow few-layered TMDCs in an epitaxial fashion.[12−17] Ye et al.[12] systematically examined the thermodynamic and kinetic controls of the vertically stacked 2D materials, where the growing conditions, such as annealing temperatures and adatom flux, play crucial roles governing the final structure. Similarly, Li et al.[13] demonstrated that the active clusters with a high diffusion barrier, for example, the ratio between metal oxides and chalcogenides, would modulate the heteroepitaxy growth direction. Besides, a wide variety of growth promoters, including aromatic derivatives and alkali metal halides, has been implemented to regulate the direction of the growth front resulting from the enhanced diffusivity of transition-metal oxide precursors. In a nutshell, this research directed at understanding the mechanisms that underly the epitaxial growth of vdW homo- and heterostructures predominately hinge on two aspects. One is the thermodynamic control of nucleation on the first TMDC epilayer, and the other is the kinetic modulation of the growth front of the second TMDC overlayer.[13−15] However, most discussion is focused on the way to overcome the exceedingly high activation energy on the basal plane of the first epilayer; little work expounds on what properties of the first epilayer will result in a different transition in the growth mode of succeeding TMDC layers.

Here we report the modulation of growth modes of succeeding TMDC layers through the creation of strain fields of the first epilayer during the epitaxy growth. The strain level of the first epilayer was engineered by the dissimilar diffusivity of metal oxide and chalcogen precursors. Comprehensive density functional theory (DFT) calculations indicate that built-in strain fields overshadow the activation energy that predominately dictates the successive growth mode of the epilayer. Atomically resolved images show that the second overlayer grown on top of the strained first epilayer has the propensity to follow both AA′ (2H) and AB (3R) stacking. Since the strain on TMDCs can be built on substrates in the CVD growth and is not limited to the current material combinations, the finding here represents a very visible nexus

https://doi.org/10.1021/acsmaterialslett.0c00554
ACS Materials Lett. 2021, 3, 442−453

between epitaxial growth and advanced nanoengineering that has the potential to open a new opportunity in the scalable production of TMDC homo- and heterostacks.

Results and Discussion

Strain on single-layer WSe_2. The process for activating the basal plane as the growth front begins with the epitaxial growth of WSe_2 monolayers by CVD that features the dual-heating zones[18] as schematically illustrated in Figure 1a. Here, the WO_3 source was located at the center of heating zone 2, and sapphire substrates were placed adjacent to the WO_3 boat. The temperature of heating zone 2 was fixed at 900 °C. The annealing temperature of heating zone 1, where Se powders are located, varied from 220 to 300 °C. We found that this Se annealing temperature is strongly associated with the shift in photoluminescence (PL) of the as-grown WSe_2 monolayer specimens that is characteristic of the structural strain (Figure S1).[19−22] When the Se annealing temperature was set at 220 °C, the as-grown WSe_2 monolayer shows an average PL emission of ~1.56 eV along the whole deposition distance. Conversely, the PL energy shifts to 1.63 eV when the Se annealing temperature is set at 300 °C. To this end, we set the annealing temperature of the first hot zone at a medium temperature of 270 °C, which in turn enables us to explore the origin of built-in strain fields. PL spectra were taken from WSe_2 specimens epitaxially grown on sapphire substrates located between the upstream and downstream regions as shown in Figure 1b. The distance between each sapphire substrate is evenly separated by 1 cm to ensure the comparison of PL spectra and the associated built-in strain fields on a fair footing. To better understand the correlative strain effect, we selected two typical samples at the opposite ends of depositing position profiles as shown in Figure 1c. Relative to the prototypical emission of ~1.66 eV of an unstrained monolayer WSe_2 reported in the literature,[20] PL spectra of WSe_2 collected near the beginning of the diffusion pathway marked as 0 cm displayed a substantial red shift of 74 meV, which can be translated into a tensile strain of ~1.2%, designated as high-tensile-strained (HTS) WSe_2.[23,24] Meanwhile, only a minor red shift of 27 meV was observed from WSe_2 specimens grown near the end of the diffusion pathway, where Se vapors become predominant. The minor shift accounts for a relatively low tensile strain of ~0.43%, namely, low-tensile-strained (LTS) WSe_2.[23,24] Intriguingly, it is found that the tensile strains in both samples relaxed after the wet transfer to freshly cleaned sapphires and their emission peaks revert back to ~1.66 eV. The tensile strain is likely built upon the cooling after growth, and it is proposed that the different strains might be related to the thermal coefficient difference between the sapphire substrate and the TMDCs grown with various conditions, which will be further discussed in the following context.

It is known that defects, trions, and band-to-band emissions all exhibit characteristic emission evolutions when excited at low temperatures.[25−27] Thus, to rule out the defect- and doping-induced shift in PL emission, we performed low-temperature PL measurements as shown in Figure S2. As suggested in the Gaussian fitted spectra, we did not observe a distinctive PL emission difference that stemmed from defect and doping contributions of both HTS and LTS WSe_2 samples. These results further attest to the fact that the peak position and intensity alteration are more likely caused by a strain-induced band variation. (See the detailed discussion in the Supporting Information, Note S1.) Furthermore, on the basis of temperature-dependent photoluminescence measurements (Figures S3 and S4), we noted that the PL energies of both samples all displayed a large redshift with increasing temperature, as a result of the increased electron−phonon interactions and the varied bonding lengths. The HTS sample can be considered that the WSe_2-sapphire exhibits a stronger interaction, while the low-tensile-strained sample LTS exhibits a much weaker (van der Waals-like) interaction. The mismatch in the thermal expansion coefficient between the first epilayer (WSe_2, (1.1−1.4) × 10^{-5}/K) and underlying substrate (sapphire, (5−8.3) × 10^{-6}/K) has profound impacts in the HTS-WSe_2 when the temperature of the PL measurement was decreased from 300 to 4 K.[28] The result is that the much wider PL energy difference between the HTS and LTS samples increased from 40 meV (300 K) to ~60 meV (4 K). To this end, we employed a modified Varshni relationship to quantitatively investigate the temperature dependence on the bandgap of strained WSe_2[29,30]

$$E_g(T) = E_g(0) - S\langle\hbar\omega\rangle\left[\coth\left(\frac{\langle\hbar\omega\rangle}{2k_BT}\right) - 1\right] \quad (1)$$

where $E_g(0)$ is the bandgap energy at absolute zero temperature, S is a dimensionless constant that represents the strength of the exciton−phonon coupling, $\langle\hbar\omega\rangle$ describes the average phonon energy involved in electron−phonon interactions, $\hbar$ is Planck's constant, and k_B is the Bolzmann constant. For HTS-WSe_2, the fitting parameter was extracted with E_g (0) ≈ 1.67 eV, S ≈ 2.07, and $\langle\hbar\omega\rangle$ ≈ 11.71 meV. A similar fitting to LTS-WSe_2 yields $E_g(0)$ ≈ 1.73 eV, S ≈ 2.66, and $\langle\hbar\omega\rangle$ ≈ 18.80 meV. By comparing these parameters, the HTS sample was found to exhibit a lower bandgap value and weaker exciton−phonon coupling, agreeing well with the previously reported results where monolayer WSe_2 is subjected to a tensile strain.[31] Meanwhile, Raman spectroscopy was used to study the spatial distribution of the built-in strain of the as-grown WSe_2. Figure 1d demonstrates that the E_{2g} peak of WSe_2 splits into two peaks and shifts to opposite directions when the growth of WSe_2 happens near the upstream. This is characteristic of the emergence of a relatively higher tensile strain,[21] which is also typically seen in CVD-grown single crystal TMDCs.[32,33] Meanwhile, when the growth of WSe_2 takes place at the downstream region, the splitting of the doublet peak gradually narrows and eventually merges at ~250 cm^{-1}, indicative of a nearly strain-free state.[21] These results collectively attest to the fact that the peak position and intensity alteration are more likely caused by a strain-induced band variation during the epitaxy.

As mentioned in the previous section, the root cause responsible for the strain variation is the combined results of subtle differences in growth environments. On the one hand, it is known that the diffusion of metal (oxide) vapors in conjunction with a significant vapor concentration drop always gives rise to a nonuniform growth distribution when the distance between metal oxide sources and designated substrates increases.[34] On the other hand, Se exhibits a low melting point (220 °C) and thus can diffuse throughout the whole furnace tube when the furnace temperature reaches 900 °C at 10 Torr.[34] We performed the evaporation of WO_3 powders in a standard growth condition except for the absence of Se (see Figure S5 for SEM images). An energy-dispersive X-ray analysis (EDX) is used to examine the relative W weight percentage of the deposited film along the path of diffusion. Figure 1e clearly shows that the concentration profile of W

https://doi.org/10.1021/acsmaterialslett.0c00554
ACS Materials Lett. 2021, 3, 442−453

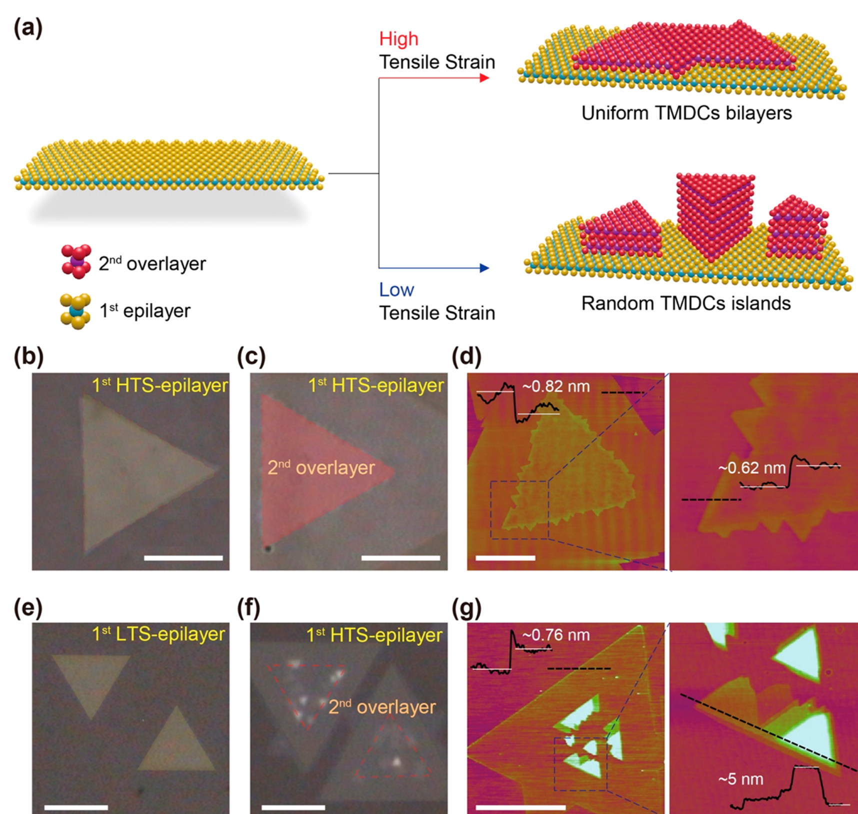

Figure 2. Growth-mode control by tensile strain. (a) Schematic representation features the growth of homogeneous second WSe_2 overlayers on the first HTS-WSe_2 epilayer in a layer-by-layer fashion. Meanwhile, island growth of multilayered clusters was found on the basal plane of the LTS-WSe_2. (b) OM image of the as-grown (0 cm) HTS-WSe_2 monolayer. (c) OM showing the formation of WSe_2 homobilayer indicated by the red, dashed triangle. (d) Corresponding AFM images of WSe_2 homobilayers as well as a close-up view of the blue-marked area. (inset) The height profile along the black dotted line. (e) OM image of the as-grown (9 cm) LTS-WSe_2 monolayer. (f) OM of WSe_2 islands formed during the second growth. (g) Corresponding AFM images reveal the multilayered islands scattered on the basal plane of the first LTS-WSe_2 epilayers. Scale bars: 5 μm.

distributes in a declining fashion, suggesting that the WO_3/Se vapor ratio scales disproportionally with the increasing distance between growth location and WO_3 source. This concentration profile shows a similar trend compared to the energy distribution shown in Figure 1b. In the meantime, we also performed the first WSe_2 epilayer growth on top of SiO_2/Si substrates as described in Figure S6 and Supporting Information, Note S4. On the basis of the experimental observations and spectroscopic characterizations, we arrived at the conclusion that the WO_3/Se vapor concentration profile enables the modulation of the strain levels in the monolayer WSe_2. Under the Se-deficient atmosphere (growth takes place near the WO_3 boat or at low Se heating temperature), the reduced W atoms may not be fully selenized and then completely converted into WSe_2. Hence, fractions of W atoms in the WSe_2 flake are chemically tethered with the oxygen-terminated sapphire surfaces at the reaction temperature. Next, the chemically pinned WSe_2 tends to develop the high built-in strain by virtue of the mismatch of the thermal expansion coefficient between that of WSe_2 and sapphire when cooling down from a high annealing temperature in the growth process.[28] At the same time, the Se-rich environment efficiently transforms WO_3 precursors to WSe_2, where the unsaturated W−O bond formation enables WSe_2 monolayers to find an energetically favorable configuration and thus leads to a low-tensile-strained monolayer. We note that the deposition temperature near the upstream location is determined to be 925 °C, and it gradually decreases to 892 °C when the depositing position moves to the downstream site. (Table S1). As discussed in Supporting Information, Note S3, the temperature difference measured at 0 and 9 cm would be a nuance (∼0.03%) and less likely to contribute to the built-in strain on the first WSe_2 epilayer.

Strain-induced epitaxy of WSe_2 homobilayers. To elucidate how a tensile strain modulates the homoepitaxial growth of WSe_2 bilayer, we applied a two-step growth procedure where a monolayer WSe_2 is grown on a sapphire followed by the van der Waals epitaxy normal to the basal plane growth front. The ability to systematically manipulate the built-in strain fields enables us to prepare the WSe_2 monolayers with various tensile strain levels as the templates to direct the growth of the subsequent second WSe_2 overlayer. As summarized in Figure 2a, the built-in strain fields of the first epilayer WSe_2 indeed play an important role in modulating the epitaxial growth front for the formation of WSe_2 homobilayers. The HTS-WSe_2 monolayer enables the layer-by-layer growth mode, whereas the LTS-WSe_2 directs the island growth mode. Figure 2b,e features the optical microscope (OM) images of the first epilayer of HTS- and LTS-WSe_2, respectively. PL and Raman measurements were used to confirm the strain uniformity and were found to follow the similar trend (see the Supporting Information, Figure S7). Here, the first HTS-WSe_2 monolayer template, even with the built-in strain of only 1.37%, evidentially and sufficiently enables the layer-by-layer growth

https://doi.org/10.1021/acsmaterialslett.0c00554
ACS Materials Lett. 2021, 3, 442−453

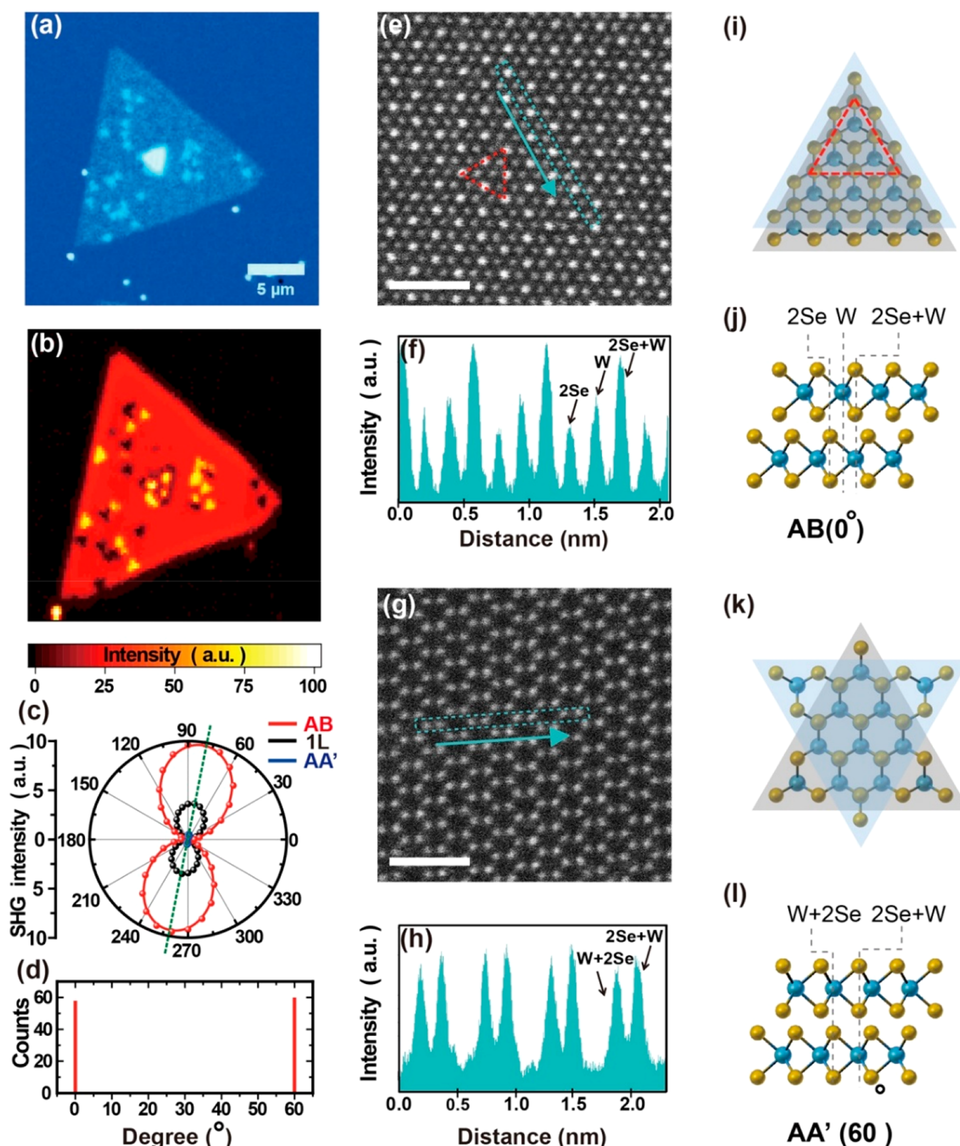

Figure 3. Stacking configuration of WSe_2homobilayers. (a) The OM image shows the inception of triangular second WSe_2 overlayers grown on the first HTS-WSe_2 epilayer. (b) The corresponding false-colored second harmonic intensity obtained by pixel-to-pixel spatial mappings in (a). (c) Polar plots of the polarization-resolved second harmonic intensity as a function of azimuthal angle φ measured from an as-grown sample. (d) Statistical histograms of the twist angles measured from hundreds of the triangular second WSe_2 overlayers. (e) HAADF-STEM image of WSe_2 homobilayers with a 0° twist angle. (f) Intensity profile along the direction of selected line in (e). (g) HAADF-STEM image of WSe_2 homobilayers with a 60° twist angle. (h) Intensity profile along the direction of selected line in (g). Atomic configuration of AB (0° twisted, 3R) stacked WSe_2 homobilayer, top view (i) and cross-sectional view (j). Atomic configuration of AA′ (60° twisted, 2H) stacked WSe_2 homobilayers, view from the top (k) and the side (l). Blue balls denote W atoms, and yellow balls represent Se atoms (i–l). Scale bar: 1 nm.

mode, whereas the epitaxy on LTS-WSe_2 (a built-in strain of 0.56%) favors the island growth mode.

After the second growth, a uniform and fully covered second overlayer of WSe_2 is epitaxially grown on top of the HTS-WSe_2 epilayer as highlighted by the dashed triangle in red in Figure 2c. The atomic force microscopy (AFM) image in Figure 2d provides the close-up view that the growth proceeds with the seeding of small triangular WSe_2 and then merges into a complete WSe_2 bilayer. The height profile determined by a blue dashed line across the interface between a substrate and the first epilayer of WSe_2 flakes is 0.82 nm, and the second layer is ∼0.62 nm, in accord with the signature thickness of monolayer WSe_2.[18] Statistically, after scouring over 1000 flakes from various epitaxy batches, all of the HTS-WSe_2 templates proceed with the layer-by-layer growth mode without exception. Figure S8 showcases the low-magnification OM image where WSe_2 homobilayers with uniform coverage are ubiquitous on all HTS-WSe_2 epilayers. To the contrary, sporadically distributed islands or multilayer clusters (thickness up to ∼10 nm) were found to scatter all over the LTS-WSe_2 flakes as shown in Figure 2f,g. Note that, although the activation of the basal plane prioritizes the vertical growth front, the underlying HTS-WSe_2 templates concurrently become discernably larger. The dashed triangles in Figure 2c,f present the size of the first epilayer in Figure 2b,e. Here, the edges of the first-layer WSe_2 serve as the nucleation sites for the second in-plane growth of WSe_2 during the ramping process.[35,36] To ensure the yield and coverage of the second

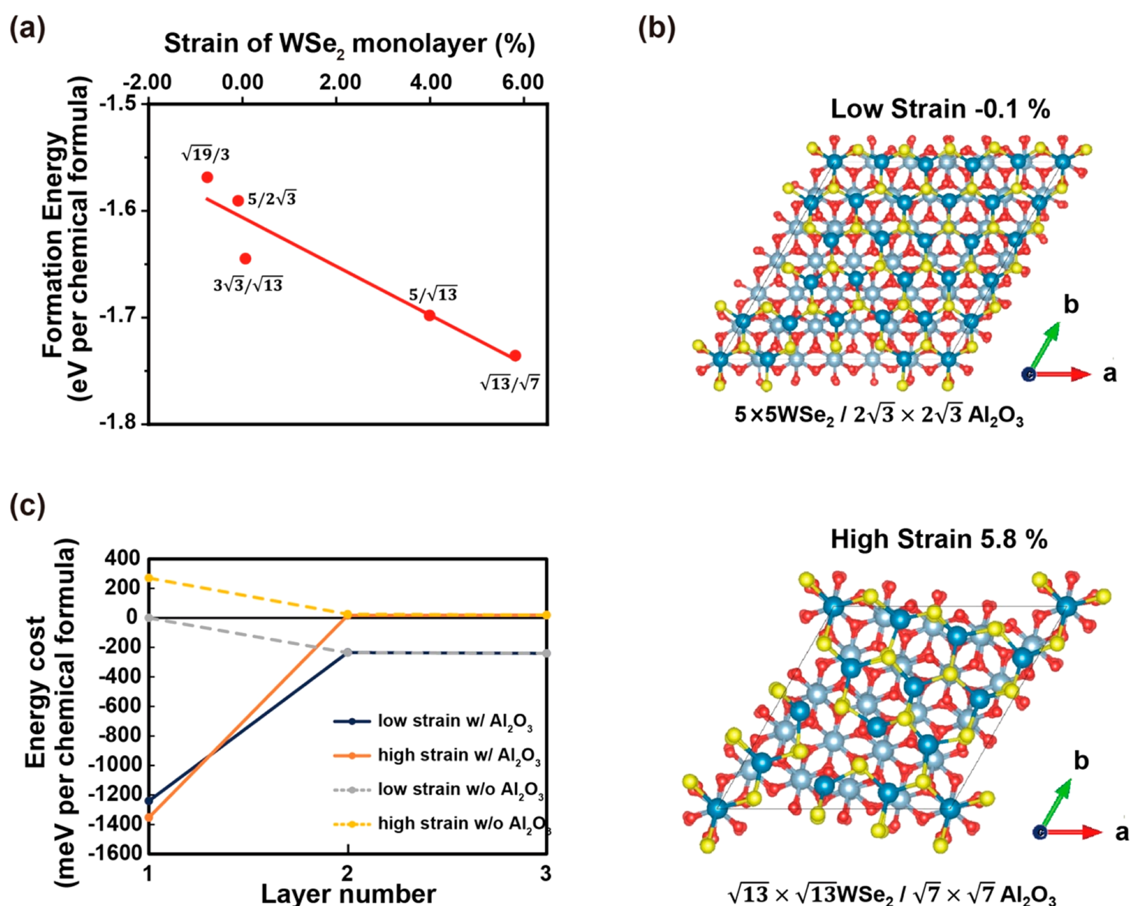

Figure 4. (a) Formation energy of monolayer WSe_2 on sapphire (Al_2O_3) superstructures with various strains. (b) Atomic models for the low-strained ($5 \times 5WSe_2/2\sqrt{3} \times 2\sqrt{3}Al_2O_3$) and high-strained ($\sqrt{13} \times \sqrt{13}WSe_2/\sqrt{7} \times \sqrt{7}Al_2O_3$) WSe_2 on Al_2O_3. (c) The calculated energy cost of the nth layer WSe_2 (with respect to the free-standing monolayer WSe_2) on two systems with substrates, defined by $E_n = E_{(n)WSe_2/Al_2O_3} - E_{(n-1)WSe_2/Al_2O_3} - E_{free-WSe_2}$ and other two without substrates.

WSe_2 overlayer, the epitaxy growth should be conducted in the high-temperature region (~900 °C) where adequate energy overcomes the nucleation barrier on the basal plane of the HTS-WSe_2 templates, therefore proceeding with the thermodynamically favorable stacking structure afterward.[12,14] An epitaxial growth at the lower temperature leads to edge-directed in-plane growth (see Figure S9) and ultimately extends to the continuous WSe_2 thin films. Figure S10 shows a typical distribution of second-growth results of HTS-WSe_2 epilayers. At the very front end, where the HTS-WSe_2 sample is placed right next to the W source, continuous multilayers (three to four layers) were developed on account of the sample precursor supply. The number of layers sequentially decreases to two to three layers and is ultimately limited to only bilayers when the HTS-WSe_2 sample gradually moves away from the W source. The same trend was also observed in the case of a low-pressure CVD monolayer growth.[37] It is noted that the scattered bright spots are thick nucleation sites. The presence of thick seeds can be suppressed efficiently by increasing the Se vapor flux or decreasing the H_2/Ar ratio to restrain the W supply during the second growth.

Characterization of as-grown multilayer WSe_2. The successful activation of the basal plane through the strain engineering of the first WSe_2 epilayer guides the layer-by-layer growth to obtain a bilayer and even the trilayer as shown in Figure S11. AFM images reveal that the triangular WSe_2 seeds the first nucleate, merges with the adjacent flakes, and ultimately forms a complete film prior to the growth of subsequent layers, closely resembling the layer-by-layer growth mode. Aside from the consistently aligned vertical growth on a basal plane, the first HTS-WSe_2 templates and the second WSe_2 overlayers are highly aligned, and the dominant twist angles/edge orientations are 0° and 60° (180°). To verify the orientation of individual flakes, the WSe_2 homobilayers were characterized by second-harmonic generation (SHG). It is known that polarization-resolved SHG is very sensitive to the crystal orientation and that the intensity profile map can be used as a descriptor for verifying spatial orientations between the first HTS-WSe_2 epilayer and the second WSe_2 overlayer. With this in mind, we specifically selected WSe_2 homobilayers with incomplete coverage of second WSe_2 overlayers as shown in Figure S11a to further enhance the fidelity of grain identification. Figure 3a,b shows the OM image and the corresponding SHG intensity map of the triangular second WSe_2 overlayers, which is independent of the polarization direction of the incident laser field with respect to the crystallographic axis. Here, the total SHG intensity of the sample was recorded. It is widely recognized that materials with the absence of inversion symmetry give rise to the SHG signal. Here, monolayer WSe_2 is characterized by the D_{3h} point-group symmetry, which enables a strong SHG signal by virtue of its broken inversion symmetry. As a result, in the case of WSe_2 homobilayers, the

https://doi.org/10.1021/acsmaterialslett.0c00554
ACS Materials Lett. 2021, 3, 442−453

enhanced SHG intensity plot (bright) that stemmed from a parallel stacking (0°) is the result of 3R stacking or AB stacking, which can be assigned to the D_{3h} point group with broken inversion symmetry. On the contrary, the much-suppressed second harmonic intensity plot (dark) taken at an antiparallel stacking (60°) is the consequence of the Bernal (2H) stacking or AA′ stacking (the D_{3d} point group) with inversion symmetry.[38] We further examined the polarization-resolved SHG as shown in Figure 3c. The polarization direction for bilayer homostructures with different twist angles seems to align well with the first HTS-WSe_2 templates, an indication of the formation of energetically and thermodynamically favorable stacking between the second overlayers on the first HTS-WSe_2 (0° or 60°). In addition, we extended the SHG measurements to different batches of WSe_2 homobilayers. From analyzing the compiled statistics shown in Figure 3d, it becomes clear that the stacking mode only shows two directions (0° twist or 60° twist) that are generally recognized as the most stable stacking in WSe_2 system.[15,39] These results are consistent with the previous observation on artificially stacked bilayer MoS_2.[38]

In parallel, the stacking configurations of the WSe_2 homobilayers were investigated by the plane-view scanning transmission electron microscopy (STEM) with the high-angle annular dark-field (HAADF) mode. This is because the Z contrast is highly dependent on the atomic numbers, making it possible to infer the detailed atomic arrangement. Here, WSe_2 homobilayers comprised of the opposite twist angle (0° and 60°) were selected (Figure S12a). Figure 3e,g features the high-resolution HAADF-STEM images taken at WSe_2 homobilayers of 0° and 60° twist angles. Distinctively different atomic patterns become discernible as a result of different stacking sequences as shown in Figure S12b,c. In the AB stacking configuration (twist angle of 0°, Figure 3i), atoms intersected by the red dashed line represent the 2Se+W overlaps. The bright spots marked in Figure 3e manifest the overlaps by means of sandwiching W atoms with two Se atoms in the vertical and aligned fashion. Furthermore, from the sectional view of the WSe_2 bilayer stacking, it becomes apparent that the upper layer slides and thus gives rise to three atomic alignments, including 2Se, W, and 2Se+W (Figure 3j). The intensity profile extracted from the selected regions in Figure 3e also follows the similar trend in terms of stacking sequence as shown in Figure 3f. Alternatively, the atomic configuration featured in Figure 3k with a 60° rotation of the hexagonal structure results in the alignment of W with Se, that is, the AA′ stacking with the atomic alignment of W+2Se and 2Se+W (Figure 3l), respectively. The intensity profile (Figure 3h) derived from Figure 3g matches well with the aforementioned atomic stacking sequence.[40] Moreover, the optical properties of as-grown WSe_2 with different layer numbers are systematically investigated (Figure S13). The results suggest that the growth front through activating the basal plane during the epitaxy has made possible the preservation of all these characteristics unique to the exfoliated benchmarks, thus distinguishing the strain-engineering approach from the other strategies.[38]

Mechanism of strain-induced bilayer WSe_2. To understand the correlation between strain and the associated growth modes, DFT computations were performed to probe the information on formation energy in the presence of strain. To this end, atomic models of monolayer WSe_2 epitaxially grown on sapphire with various degrees of the magnitude of built-in strain ranging from −1% to 6% were constructed. The formation energy is calculated for each superstructure that sits at the lowest energy among various atomic registries by sliding the layer surface with respect to the substrate. The calculated formation energy on the basal plane, $E_f = E_{WSe_2/Al_2O_3} - E_{WSe_2} - E_{Al_2O_3}$, is found to decrease linearly as strain increases (Figure 4a), suggesting that the high tensile strain indeed arises from the strong interaction between the WSe_2 and sapphire substrate. The formation energy E_f is known to be associated with the change of Gibbs free energy per unit volume of the solid phase, ΔG_v. The change of volume of Gibbs free energy can be expressed as $\Delta G^* = \left(\frac{16\pi\gamma Vf}{3(\Delta G_v + w)^2}\right) \times \left(\frac{2 - 3\cos\theta + \cos^3\theta}{4}\right)$ where γ is the surface tension, θ represents the contact angle, and w denotes the strain energy per unit volume generated by the stress in the epitaxy. When the strain energy per unit volume generated by the disproportional concentration profile of WO_3/Se precursor vapors is included, the overall energy barrier to nucleation increases, because the sign of ΔG_v is negative, and the sign of strain energy is positive.

With this in mind, as shown in Figure 4b, we investigate the energetics of the layer-by-layer growth mode of the subsequent second WSe_2 overlayer. Two atomic models for the LTS ($5 \times 5WSe_2/2\sqrt{3} \times 2\sqrt{3}Al_2O_3$) and HTS ($\sqrt{13} \times \sqrt{13}WSe_2/\sqrt{7} \times \sqrt{7}Al_2O_3$) WSe_2 on sapphire corresponds to the two extremities of the WSe_2-sapphire interactions: (i) nearly strain-free (−0.1%) and (ii) extremely high orders of magnitude of strain level of 5.8%, respectively. Figure 4c shows the calculated energy cost of the formation of the nth (n = 1,2,3) WSe_2 overlayer (with regard to free-standing single layer) on the two aforementioned systems, defined by $E_n = E_{(n)WSe_2/Al_2O_3} - E_{(n-1)WSe_2/Al_2O_3} - E_{free-WSe_2}$. Another two reference cases, HTS-WSe_2 and LTS-WSe_2 in a freestanding form, that is, without the supporting Al_2O_3 substrates, are also included for comparison. It is found that the energetic landscape of the subsequent epilayer always shifts toward the lower end in the less-strained system (the difference is ∼260−270 meV per chemical formula for n = 2 and 3). Meanwhile, after including the underlying Al_2O_3 growth substrates, the energy cost of the first WSe_2 epilayer for the high tensile strain case becomes even lower than that of a low-strain case, shifting by 112 meV per chemical formula. This shift in energy cost thus suggests the presence of a strong interaction between the first WSe_2 epilayer and Al_2O_3 in the high tensile strain cases. (Note that the distance between the bottom Se layer and the O-termination surface is 1.77 and 1.7 Å for low- and high-strain systems.) The energy cost for adding second and third WSe_2 overlayers becomes nearly identical with or without substrates (Figure 4). In parallel, contributions to the layer-by-layer energy cost of the WSe_2/Al_2O_3 system are twofold: substrate interaction and strain effect, with the former being negative, and the latter being positive. In the stronger interaction with an underlying substrate in a HTS-WSe_2-induced Frank−van der Merwe (layer-by-layer) growth mode,[41] adatoms attach preferentially to surface sites resulting in a laterally grown film prior to the growth of subsequent layers along the vertical direction. Antithetically, a negligible strain in LTS-WSe_2 leads to a Volmer−Weber (nucleation-to-island) growth,[42] indicating a very weak interaction with the surface, such that adatom−adatom interactions are stronger

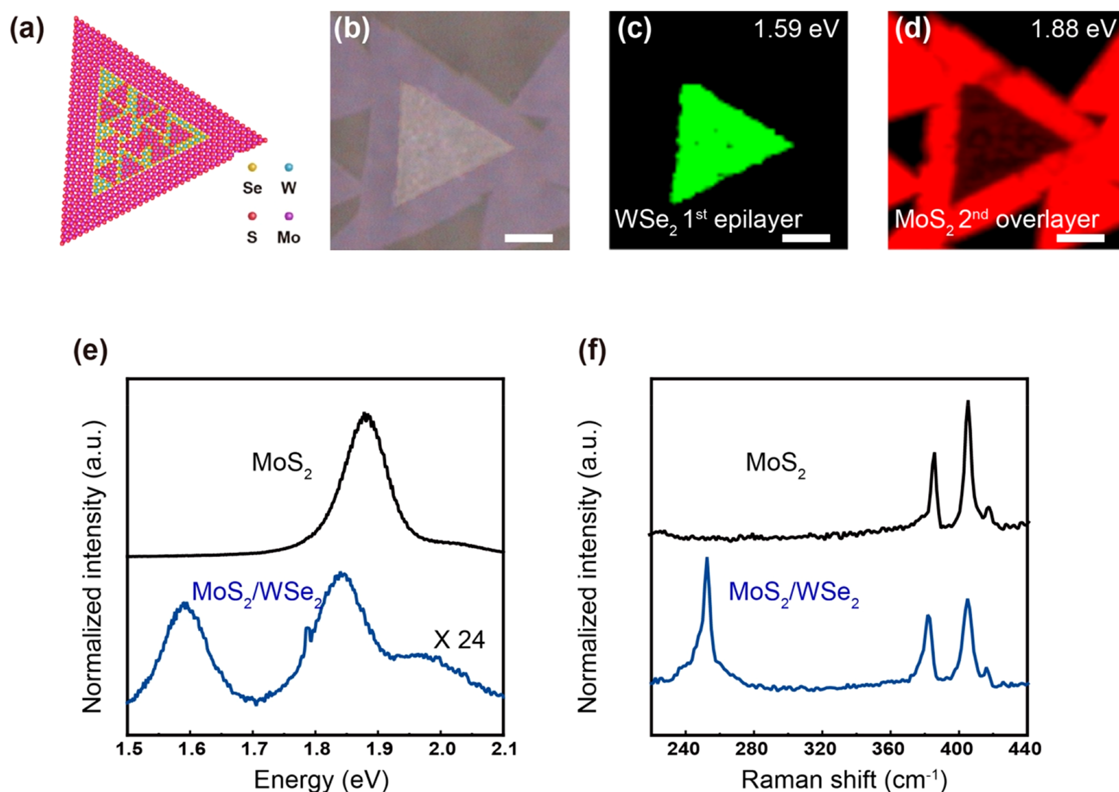

Figure 5. MoS_2/WSe_2 heterostructure obtained from the first HTS-WSe_2. (a) Schematic illustration of atomic structures and (b) OM image of vertical and lateral MoS_2/WSe_2 heterostructures. (c, d) The corresponding PL mapping images at 1.59 and 1.88 eV, respectively. (e) PL spectra and (f) Raman spectra corrected from the core (blue) and surrounding (black) regions. Scale bars: 5 μm.

than those of the adatom with the surface, resulting in the vertical growth with adatom clusters or islands. As a result, the layer-by-layer vertical growth of WSe_2 bilayers is energetically preferred at the beginning of the nucleation stage and becomes thermodynamically stable at the end of the epitaxial growth by virtue of compensating the energy cost induced by the high tensile strain ($E_{2,3} > 0$). For low-strain (nearly strain-free) systems, the total energy cost is always negative, and therefore the growth of a subsequent second WSe_2 overlayer favors the nucleation-to-island mode. Our experimental observation and simulations agree well with the above thin-film growth models.

Growth and Characterization of MoS_2/WSe_2 Heterobilayers. Because our strain-engineering epitaxy is directed by the built-in strain fields, intrinsic to the 2D TMDC growth, its use is not limited to the WSe_2−WSe_2 homobilayers reported here. Instead, it could be generalized for epitaxy growth of vdW heterobilayers with atomically thin p−n junctions. Here, combined with the understanding of the nucleation and growth characteristics on an HTS-WSe_2 template, we expanded the strain-induced epitaxy growth to include MoS_2/WSe_2 p−n heterobilayers. To this end, HTS-WSe_2 first epilayers were again featured as the strained template for the subsequent growth of second MoS_2 overlayers. Note that a two-step growth in different furnaces is used to afford the heterostructures without cross contamination at the atomically thin p−n interfaces. The growth temperature of second MoS_2 overlayers is set at 750−760 °C under 30 Torr with Ar as the carrier gas. Figure 5a schematically illustrates the sequential epitaxy growth of second MoS_2 overlayers. Both vertical and lateral epitaxy growths of MoS_2 on the HTS-WSe_2 templates are observed with the vertical growth front (basal plane) outweighing the lateral counterparts (edges). This can be understood from the epitaxial point of view that the formation of lateral p−n junctions takes place during the ramping of annealing temperatures for the second growth.[35,43] We specifically selected WSe_2/MoS_2 heterobilayers with an incomplete coverage of a second MoS_2 epilayer as a result of PL quenching, which can be leveraged as a descriptor to identify the location of second MoS_2 epilayers. Figure 5b shows the OM image of the as-grown MoS_2/WSe_2 heterobilayers. The distribution of the first WSe_2 template and the second MoS_2 overlayer was further examined by PL intensity maps at 1.59 eV (wavelength of 780 nm) and 1.88 eV (wavelength of 660 nm), characteristic of the direct excitonic transitions in both MoS_2 and WSe_2. A PL mapping of relevant PL characteristics, including MoS_2 in green (Figure 5c) and WSe_2 in red (Figure 5d), evidentially proves the successful out-of-plane growth of n-type MoS_2 on the basal plane of p-type WSe_2. In addition, the PL spectra in Figure 5e reveal diverse PL emission peaks at the core (blue) and from the surrounding (black) regions. The black curve with a prominent emission peak at 1.88 eV represents the direct bandgap excitonic peak of monolayer MoS_2. Meanwhile, the emergence of two relatively weak peaks in blue (1.59 vs 1.85 eV) was observed in the core region. The peak assigned at 1.59 eV corresponds to the combination of intralayer excitonic emission from the underlying WSe_2 epilayer (X_{WSe2} at 1.61 eV) and the MoS_2/WSe_2 interlayer exiton ($X_{MoS2/WSe2}$ at 1.58 eV), as shown in Figure S14.[44] The considerable deviation and intensity quenching of PL emission can be translated into the strong interlayer coupling and charge transfer, characteristic of the type II heterostructures.[45] Similarly, Raman spectra acquired

https://doi.org/10.1021/acsmaterialslett.0c00554
ACS Materials Lett. 2021, 3, 442−453

from the core region (black) and surrounding (blue) area of the MoS_2/WSe_2 heterostructures were summarized in Figure 5f. Two predominant peaks at 405 and 385 cm^{-1}, which correspond to the A_{1g} and E_{2g} modes of monolayer MoS_2, arise from the surrounding. Nevertheless, the core region exhibits both characteristic peaks of MoS_2 and WSe_2 (250 cm^{-1}, E_{2g} mode), respectively. The presence of relevant Raman characteristics in tandem with representative features from both PL spectra and mappings collectively manifests the applicability and generality of a strain-induced epitaxy growth of heterobilayers with atomically thin and clean p−n interfaces. A wide variety of artificial TMDC heterostackings with control over the number of layers, uniformity, coverage, and intrinsic material properties can thus be epitaxially grown for a myriad of electronic and optoelectronic applications.

Conclusions. In conclusion, we have demonstrated that built-in strain fields in 2D TMDCs play a crucial role in activating the out-of-plane growth front for affording homo- and hetero-bilayers. With the consistent agreement between DFT simulations, experimental observations, and spectroscopic characterizations, our findings elucidate general rules for a strain-driven epitaxy growth of homo- and heterobilayers: (1) the overall energy barrier to rampant nucleation increases because of the presence of strain energy that reconciles the adverse impact of ΔG_v. The result is the activation of the growth front on the basal plane where epitaxy of bilayer proceeds, (2) built-in strain fields in the first WSe_2 epilayers stem from the combined effects of local chemical environments and can be systematically modulated in situ during the epitaxy growth, (3) the stacking of homo- and heteroepilayers predominately follows AB (0° twisted, 3R) and AA′ (60° twisted, 2H) according to the analyses of SHG measurement and HAADF-STEM images, and (4) this strain-modulated epitaxy can be a general platform for extending libraries of vdW homo- and heterobilayers. Such an understanding not only provides fundamental insights into the knowledge for the vapor-phase epitaxy of 2D layers but opens new inroads in the direct growth of vdW homo- and heterobilayers with control over the bilayer coverage and content in tandem with the preservation of electrically addressable and spectroscopically tractable interfaces in a potentially scalable and industry-compatible fashion.

Materials and Methods

Growth of monolayer, WSe_2 homobilayers, and MoS_2/WSe_2 heterobilayers. First, the epitaxy growth of single-crystal first WSe_2 epilayers was adopted from the previous work.[18] In essence, WO_3 (Sigma-Aldrich, 99.9%) powders were placed in a ceramic boat that was located at the center of the furnace. The sapphire substrates were located in the downstream side adjacent to the ceramic boat as shown in Figure 1. The Se powders (Sigma-Aldrich, 99.99%) were annealed by a heating tape at the upstream side, and the resulting Se vapors were transported by an Ar/hydrogen (H_2) mixture gas (66 to 5 sccm). The furnace was then heated to 900 °C with a heating rate of 25 °C/min at 10 Torr. The duration of the epitaxy growth of the first WSe_2 was ∼15 min, subjected to the variation in ramping rate and loading of precursors. Upon completion, the system was naturally cooled to room temperature. The production of both HTS-WSe_2 and LTS-WSe_2 was accomplished by adjusting the precursor ratio between W and Se. For obtaining the WSe_2 homobilayers, the resultant HTS-WSe_2 along with the sapphire substrate was directly used as the template and was placed in the downstream side. Note that the growth of a second epilayer was performed under a Se-rich environment. Through control of the growth time, a fully covered WSe_2 homobilayer film can be achieved. In the case of synthesizing the MoS_2/WSe_2 heterobilayers, the as-grown HTS-WSe_2 flakes/films were transferred into another CVD furnace to avoid cross-contamination. The furnace temperature was set as 800 °C with the surface temperature of growth substrate measured at ∼750−760 °C, and the duration of the epitaxy growth lasted for 10 min. Importantly, in the MoS_2 furnace, S powders (Sigma-Aldrich, 99.9%) and MoO_3 powders (Sigma-Aldrich, 99.9%) were used as precursors. The flow of carrier gas (Ar) was carefully maintained at 70 sccm, and the pressure was controlled at 30 Torr.

Raman & photoluminescence characterization. The Raman and photoluminescence (PL) spectra on WSe_2 homobilayers and WSe_2/MoS_2 heterobilayers were collected using a Witec alpha 300 confocal Raman microscope equipped with a RayShield coupler. A 532 nm solid-state laser was the excitation source. The excitation light with a power of 2.5 mW was focused onto the sample by a 100× objective lens (numerical aperture (NA) = 0.9). The signal was collected by the same objective lens, analyzed by a 0.75 m monochromator, and detected by a liquid-nitrogen-cooled charge-coupled device (CCD) camera. The atomic force microscopy (Cypher ES-Asylum Research Oxford Instruments) characterizations were conducted with Olympus (OMCLAC240TS) Al-coated silicon cantilevers. The resonance frequency was ∼70 kHz, the spring constant was ∼2 N/m, and the tip curvature radius was ∼7 nm. The temperature-dependent PL spectra on monolayer HTS-WSe_2 and LTS-WSe_2 flakes was measured by a microphotoluminescence setup integrated in a cryogen-free cryostat with a base temperature of 4.2 K. A He−Ne laser with a wavelength of 632.8 nm was focused by a 100× objective lens (NA = 0.82) to excite the WSe_2 flakes. The PL signals were collected by the same objective lens and sent to a liquid-nitrogen-cooled CCD detector.

Second-harmonic generation measurements. SHG spectroscopy was conducted by a backscattering optical microscope at room temperature.[38] The fundamental field was provided by a mode-locked Ti:sapphire pulsed laser (870 nm) and focused on the sample surface by a 100× objective lens (NA = 0.9). The backscattered SHG signals were collected by the same objective lens, analyzed by a 0.75 m monochromator, and detected by a liquid-nitrogen-cooled CCD camera. The polarization of the fundamental laser (SHG signal) was selected (analyzed) by combining a linear polarizer and a half-wave plate. For spatial SHG mappings, the sample was mounted on a motorized x-y scanning stage with the high repeatability of 0.25 μm.

Scanning transmission electron microscopy. The homo- and heterobilayer samples for STEM were prepared by wet-transfer methods. Specifically, poly(methyl methacrylate) (PMMA) was spin-coated onto the as-grown WSe_2 homobilayer samples as a supporting substrate. The PMMA/WSe_2 homobilayer composites were fully soaked into HF solution, leaving behind the WSe_2 homobilayers. After a rinse with copious amounts of deionized water (DI-H_2O), suspended WSe_2 homobilayers were scooped onto transmission electron microscopy (TEM) grids. To enhance the adhesion between WSe_2 homobilayer samples and the underlying TEM grids, an additional annealing was performed at 50 °C for 1 h. Then the residual PMMA was fully removed by a thorough acetone rinse. The HAADF-

STEM imaging was conducted at 80 kV using a JEOL ARM 200F transmission electron microscope (80–200 kV). The TEM is equipped with a Cs (spherical aberration) corrector and a high brightness cold field-emission gun (C-FEG), and the STEM detector is made of yttrium aluminum perovskite (YAP).

Density function theory simulation. The first-principles calculations were performed with DFT as implemented in the Vienna Ab initio Simulation Package (VASP).[46] The interaction between electrons and ionic cores was approximated by the projector augmented wave method, and the exchange-correlation potential was described by the PBE-GGA,[47] with the vdW correction vdW-DF (optB86) functionals.[48] A slab model is used for simulation with a vacuum thickness larger than 18 Å to eliminate the spurious interaction, and the plane waves energy cutoff is 400 eV. The structure was fully relaxed until the change of the energy and the force reached 10^{-5} eV per 1 × 1 cell and 10^{-3} eV/Å, respectively. A 2 × 2 × 1 and 3 × 3 × 1 k-grid was used for low-strained ($5 \times 5WSe_2/2\sqrt{3} \times 2\sqrt{3}$ Al_2O_3) and high-strained ($\sqrt{13} \times \sqrt{13}WSe_2/\sqrt{7} \times \sqrt{7}$ Al_2O_3) systems, with an interlayer distance of 1.77 and 1.70 Å between the WSe_2 and Al_2O_3 and an interlayer distance between 6.58 and 6.5 Å for WSe_2 and WSe_2. The lattice constants of WSe_2 and sapphire used for calculations are 3.28 and 4.73 Å.

■ ASSOCIATED CONTENT

Supporting Information

The Supporting Information is available free of charge at https://pubs.acs.org/doi/10.1021/acsmaterialslett.0c00554.

> Plot of energy distribution, discussion of temperature-dependent PL spectra, SEM images, discussion of the modified growth process, discussion of mismatch in the thermal expansion coefficient, temperature variation along diffusion pathway, microscopy and spectroscopy characterizations, discussion of optical properties (PDF)

■ AUTHOR INFORMATION

Corresponding Authors

Vincent Tung − *Physical Sciences and Engineering Division, King Abdullah University of Science and Technology, Thuwal 23955-6900, Kingdom of Saudi Arabia;* orcid.org/0000-0003-3230-0932; Email: vincent.tung@kaust.edu.sa

Lain-Jong Li − *Physical Sciences and Engineering Division, King Abdullah University of Science and Technology, Thuwal 23955-6900, Kingdom of Saudi Arabia; School of Materials Science and Engineering, University of New South Wales, Sydney 2052, New South Wales, Australia*; Email: lance.li@kaust.edu.sa

Authors

Yi Wan − *Physical Sciences and Engineering Division, King Abdullah University of Science and Technology, Thuwal 23955-6900, Kingdom of Saudi Arabia;* orcid.org/0000-0002-6202-4193

Jing-Kai Huang − *School of Materials Science and Engineering, University of New South Wales, Sydney 2052, New South Wales, Australia*

Chih-Piao Chuu − *Institute of Atomic and Molecular Sciences, Academia Sinica, Taipei 11529, Taiwan*

Wei-Ting Hsu − *Department of Physics, National Tsing Hua University, Hsinchu 30010, Taiwan*

Chien-Ju Lee − *Department of Physics, National Tsing Hua University, Hsinchu 30010, Taiwan*

Areej Aljarb − *Physical Sciences and Engineering Division, King Abdullah University of Science and Technology, Thuwal 23955-6900, Kingdom of Saudi Arabia*

Chun-Wei Huang − *Material and Chemical Research Laboratories, Nanotechnology Research Center, Industrial Technology Research Institute, Hsinchu 310, Taiwan*

Ming-Hui Chiu − *Physical Sciences and Engineering Division, King Abdullah University of Science and Technology, Thuwal 23955-6900, Kingdom of Saudi Arabia;* orcid.org/0000-0003-3753-8149

Hao-Ling Tang − *Physical Sciences and Engineering Division, King Abdullah University of Science and Technology, Thuwal 23955-6900, Kingdom of Saudi Arabia*

Ci Lin − *Physical Sciences and Engineering Division, King Abdullah University of Science and Technology, Thuwal 23955-6900, Kingdom of Saudi Arabia*

Xuechun Zhang − *Physical Sciences and Engineering Division, King Abdullah University of Science and Technology, Thuwal 23955-6900, Kingdom of Saudi Arabia*

Ching-Ming Wei − *Institute of Atomic and Molecular Sciences, Academia Sinica, Taipei 11529, Taiwan;* orcid.org/0000-0003-3984-4422

Sean Li − *School of Materials Science and Engineering, University of New South Wales, Sydney 2052, New South Wales, Australia*

Wen-Hao Chang − *Department of Physics, National Tsing Hua University, Hsinchu 30010, Taiwan;* orcid.org/0000-0003-4880-6006

Complete contact information is available at: https://pubs.acs.org/10.1021/acsmaterialslett.0c00554

Notes

The authors declare no competing financial interest.

■ ACKNOWLEDGMENTS

V.T. and L.-J.L. acknowledge the support from King Abdullah University of Science and Technology (KAUST) Office of Sponsored Research (OSR) under Award No. OSR-2018-CARF/CCF-3079. V.T. is grateful for the support from KAUST Catalysis Center. A.A. and M.-H.C. are supported by KAUST Solar Center. W.H.C. acknowledges the support from the Ministry of Science and Technology of Taiwan (MOST-108-2119-M-009-011-MY3, MOST-107-2112-M-009-024-MY3) and from the CEFMS of NCTU supported by the Ministry of Education of Taiwan. V.T. and Y.W. are indebted to the support from Core Lab in KAUST and the fruitful discussions in DFT with Dr. Z. Cao.

■ REFERENCES

(1) Wen, W.; Wu, L.; Yu, T. Excitonic Lasers in Atomically Thin 2D Semiconductors. *ACS Materials Letters* **2020**, *2* (10), 1328−1342.

(2) Yang, C.-W.; Tang, H.-L.; Sattar, S.; Chiu, M.-H.; Wan, Y.; Chen, C.-H.; Kong, J.; Huang, K.-W.; Li, L.-J.; Tung, V. Epitaxial Growth and Determination of Band Alignment of Bi2Te3−WSe2 Vertical van der Waals Heterojunctions. *ACS Materials Letters* **2020**, *2* (10), 1351−1359.

(3) Novoselov, K. S.; Mishchenko, A.; Carvalho, A.; Castro Neto, A. H. 2D materials and van der Waals heterostructures. *Science* **2016**, *353* (6298), aac9439.

(4) Lee, C.-H.; Lee, G.-H.; van der Zande, A. M.; Chen, W.; Li, Y.; Han, M.; Cui, X.; Arefe, G.; Nuckolls, C.; Heinz, T. F.; Guo, J.; Hone,

J.; Kim, P. Atomically thin p−n junctions with van der Waals heterointerfaces. *Nat. Nanotechnol.* **2014**, *9* (9), 676−681.
(5) Howell, S. L.; Jariwala, D.; Wu, C.-C.; Chen, K.-S.; Sangwan, V. K.; Kang, J.; Marks, T. J.; Hersam, M. C.; Lauhon, L. J. Investigation of band-offsets at monolayer−multilayer MoS2 junctions by scanning photocurrent microscopy. *Nano Lett.* **2015**, *15* (4), 2278−2284.
(6) Brar, V. W.; Sherrott, M. C.; Jariwala, D. Emerging photonic architectures in two-dimensional opto-electronics. *Chem. Soc. Rev.* **2018**, *47* (17), 6824−6844.
(7) Natori, K. Ballistic metal-oxide-semiconductor field effect transistor. *J. Appl. Phys.* **1994**, *76* (8), 4879−4890.
(8) Kim, S.; Konar, A.; Hwang, W.-S.; Lee, J. H.; Lee, J.; Yang, J.; Jung, C.; Kim, H.; Yoo, J.-B.; Choi, J.-Y.; Jin, Y. W.; Lee, S. Y.; Jena, D.; Choi, W.; Kim, K. High-mobility and low-power thin-film transistors based on multilayer MoS2 crystals. *Nat. Commun.* **2012**, *3*, 1011.
(9) Choi, W.; Cho, M. Y.; Konar, A.; Lee, J. H.; Cha, G.-B.; Hong, S. C.; Kim, S.; Kim, J.; Jena, D.; Joo, J.; Kim, S. High-Detectivity Multilayer MoS2 Phototransistors with Spectral Response from Ultraviolet to Infrared. *Adv. Mater.* **2012**, *24* (43), 5832−5836.
(10) Lee, H. S.; Min, S.-W.; Chang, Y.-G.; Park, M. K.; Nam, T.; Kim, H.; Kim, J. H.; Ryu, S.; Im, S. MoS2 nanosheet phototransistors with thickness-modulated optical energy gap. *Nano Lett.* **2012**, *12* (7), 3695−3700.
(11) Liu, K.; Yan, Q.; Chen, M.; Fan, W.; Sun, Y.; Suh, J.; Fu, D.; Lee, S.; Zhou, J.; Tongay, S.; Ji, J.; Neaton, J. B.; Wu, J. Elastic Properties of Chemical-Vapor-Deposited Monolayer MoS2, WS2, and Their Bilayer Heterostructures. *Nano Lett.* **2014**, *14* (9), 5097−5103.
(12) Ye, H.; Zhou, J.; Er, D.; Price, C. C.; Yu, Z.; Liu, Y.; Lowengrub, J.; Lou, J.; Liu, Z.; Shenoy, V. B. Toward a Mechanistic Understanding of Vertical Growth of van der Waals Stacked 2D Materials: A Multiscale Model and Experiments. *ACS Nano* **2017**, *11* (12), 12780−12788.
(13) Li, F.; Feng, Y.; Li, Z.; Ma, C.; Qu, J.; Wu, X.; Li, D.; Zhang, X.; Yang, T.; He, Y.; Li, H.; Hu, X.; Fan, P.; Chen, Y.; Zheng, B.; Zhu, X.; Wang, X.; Duan, X.; Pan, A. Rational Kinetics Control toward Universal Growth of 2D Vertically Stacked Heterostructures. *Adv. Mater.* **2019**, *31* (27), 1901351.
(14) Shang, S. L.; Lindwall, G.; Wang, Y.; Redwing, J. M.; Anderson, T.; Liu, Z. K. Lateral Versus Vertical Growth of Two-Dimensional Layered Transition-Metal Dichalcogenides: Thermodynamic Insight into MoS2. *Nano Lett.* **2016**, *16* (9), 5742−50.
(15) Zhang, X.; Nan, H.; Xiao, S.; Wan, X.; Gu, X.; Du, A.; Ni, Z.; Ostrikov, K. K. Transition metal dichalcogenides bilayer single crystals by reverse-flow chemical vapor epitaxy. *Nat. Commun.* **2019**, *10* (1), 598.
(16) Han, A.; Aljarb, A.; Liu, S.; Li, P.; Ma, C.; Xue, F.; Lopatin, S.; Yang, C.-W.; Huang, J.-K.; Wan, Y.; Zhang, X.; Xiong, Q.; Huang, K.-W.; Tung, V.; Anthopoulos, T. D.; Li, L.-J. Growth of 2H stacked WSe2 bilayers on sapphire. *Nanoscale Horizons* **2019**, *4* (6), 1434−1442.
(17) Jeon, J.; Jang, S. K.; Jeon, S. M.; Yoo, G.; Jang, Y. H.; Park, J. H.; Lee, S. Layer-controlled CVD growth of large-area two-dimensional MoS2 films. *Nanoscale* **2015**, *7* (5), 1688−95.
(18) Huang, J.-K.; Pu, J.; Hsu, C.-L.; Chiu, M.-H.; Juang, Z.-Y.; Chang, Y.-H.; Chang, W.-H.; Iwasa, Y.; Takenobu, T.; Li, L.-J. Large-Area Synthesis of Highly Crystalline WSe2Monolayers and Device Applications. *ACS Nano* **2014**, *8* (1), 923−930.
(19) Johari, P.; Shenoy, V. B. Tuning the electronic properties of semiconducting transition metal dichalcogenides by applying mechanical strains. *ACS Nano* **2012**, *6* (6), 5449−5456.
(20) Hsu, W. T.; Lu, L. S.; Wang, D.; Huang, J. K.; Li, M. Y.; Chang, T. R.; Chou, Y. C.; Juang, Z. Y.; Jeng, H. T.; Li, L. J.; Chang, W. H. Evidence of indirect gap in monolayer WSe2. *Nat. Commun.* **2017**, *8* (1), 929.
(21) Desai, S. B.; Seol, G.; Kang, J. S.; Fang, H.; Battaglia, C.; Kapadia, R.; Ager, J. W.; Guo, J.; Javey, A. Strain-induced indirect to direct bandgap transition in multilayer WSe2. *Nano Lett.* **2014**, *14* (8), 4592−7.
(22) Ahn, G. H.; Amani, M.; Rasool, H.; Lien, D.-H.; Mastandrea, J. P.; Ager, J. W., III; Dubey, M.; Chrzan, D. C.; Minor, A. M.; Javey, A. Strain-engineered growth of two-dimensional materials. *Nat. Commun.* **2017**, *8* (1), 608.
(23) Frisenda, R.; Drüppel, M.; Schmidt, R.; Michaelis de Vasconcellos, S.; Perez de Lara, D.; Bratschitsch, R.; Rohlfing, M.; Castellanos-Gomez, A. Biaxial strain tuning of the optical properties of single-layer transition metal dichalcogenides. *npj 2D Materials and Applications* **2017**, *1* (1), 10.
(24) Schmidt, R.; Niehues, I.; Schneider, R.; Drüppel, M.; Deilmann, T.; Rohlfing, M.; De Vasconcellos, S. M.; Castellanos-Gomez, A.; Bratschitsch, R. Reversible uniaxial strain tuning in atomically thin WSe2. *2D Mater.* **2016**, *3* (2), No. 021011.
(25) Tongay, S.; Suh, J.; Ataca, C.; Fan, W.; Luce, A.; Kang, J. S.; Liu, J.; Ko, C.; Raghunathanan, R.; Zhou, J.; Ogletree, F.; Li, J.; Grossman, J. C.; Wu, J. Defects activated photoluminescence in two-dimensional semiconductors: interplay between bound, charged, and free excitons. *Sci. Rep.* **2013**, *3*, 2657.
(26) Jones, A. M.; Yu, H.; Ghimire, N. J.; Wu, S.; Aivazian, G.; Ross, J. S.; Zhao, B.; Yan, J.; Mandrus, D. G.; Xiao, D.; Yao, W.; Xu, X. Optical generation of excitonic valley coherence in monolayer WSe2. *Nat. Nanotechnol.* **2013**, *8*, 634.
(27) Sharma, R.; Pandey, J.; Sahoo, K. R.; Rana, K. S.; Biroju, R. K.; Theis, W.; Soni, A.; Narayanan, T. N. Spectroscopic correlation of chalcogen defects in atomically thin MoS2 (1− x) Se2x alloys. *J. Phys. Mater.* **2020**, *3* (4), No. 045001.
(28) Lippert, S.; Schneider, L. M.; Renaud, D.; Kang, K. N.; Ajayi, O.; Kuhnert, J.; Halbich, M.-U.; Abdulmunem, O. M.; Lin, X.; Hassoon, K.; Edalati-Boostan, S.; Kim, Y. D.; Heimbrodt, W.; Yang, E.-H.; Hone, J. C.; Rahimi-Iman, A. Influence of the substrate material on the optical properties of tungsten diselenide monolayers. *2D Mater.* **2017**, *4* (2), No. 025045.
(29) O'Donnell, K.; Chen, X. Temperature dependence of semiconductor band gaps. *Appl. Phys. Lett.* **1991**, *58* (25), 2924−2926.
(30) Tongay, S.; Zhou, J.; Ataca, C.; Lo, K.; Matthews, T. S.; Li, J.; Grossman, J. C.; Wu, J. Thermally driven crossover from indirect toward direct bandgap in 2D semiconductors: MoSe2 versus MoS2. *Nano Lett.* **2012**, *12* (11), 5576−5580.
(31) Niehues, I.; Schmidt, R.; Druppel, M.; Marauhn, P.; Christiansen, D.; Selig, M.; Berghauser, G.; Wigger, D.; Schneider, R.; Braasch, L.; Koch, R.; Castellanos-Gomez, A.; Kuhn, T.; Knorr, A.; Malic, E.; Rohlfing, M.; Michaelis de Vasconcellos, S.; Bratschitsch, R. Strain Control of Exciton-Phonon Coupling in Atomically Thin Semiconductors. *Nano Lett.* **2018**, *18* (3), 1751−1757.
(32) Xu, R.; Pang, F.; Pan, Y.; Lun, Y.; Meng, L.; Zheng, Z.; Xu, K.; Lei, L.; Hussain, S.; Li, Y. J.; Sugawara, Y.; Hong, J.; Ji, W.; Cheng, Z. Atomically Asymmetric Inversion Scales up to Mesoscopic Single-Crystal Monolayer Flakes. *ACS Nano* **2020**, *14* (10), 13834−13840.
(33) Zhang, K.; Hu, S.; Zhang, Y.; Zhang, T.; Zhou, X.; Sun, Y.; Li, T.-X.; Fan, H. J.; Shen, G.; Chen, X.; Dai, N. Self-Induced Uniaxial Strain in MoS2Monolayers with Local van der Waals-Stacked Interlayer Interactions. *ACS Nano* **2015**, *9* (3), 2704−2710.
(34) Aljarb, A.; Cao, Z.; Tang, H. L.; Huang, J. K.; Li, M.; Hu, W.; Cavallo, L.; Li, L. J. Substrate Lattice-Guided Seed Formation Controls the Orientation of 2D Transition-Metal Dichalcogenides. *ACS Nano* **2017**, *11* (9), 9215−9222.
(35) Li, M.-Y.; Shi, Y.; Cheng, C.-C.; Lu, L.-S.; Lin, Y.-C.; Tang, H.-L.; Tsai, M.-L.; Chu, C.-W.; Wei, K.-H.; He, J.-H.; Chang, W.-H.; Suenaga, K.; Li, L.-J. Epitaxial growth of a monolayer WSe2-MoS2 lateral p−n junction with an atomically sharp interface. *Science* **2015**, *349* (6247), 524−528.
(36) Li, M.-Y.; Pu, J.; Huang, J.-K.; Miyauchi, Y.; Matsuda, K.; Takenobu, T.; Li, L.-J. Self-Aligned and Scalable Growth of Monolayer WSe2−MoS2 Lateral Heterojunctions. *Adv. Funct. Mater.* **2018**, *28* (17), 1706860.
(37) Chiu, M.-H.; Tang, H.-L.; Tseng, C.-C.; Han, Y.; Aljarb, A.; Huang, J.-K.; Wan, Y.; Fu, J.-H.; Zhang, X.; Chang, W.-H.; Muller, D. A.; Takenobu, T.; Tung, V.; Li, L.-J. Metal-Guided Selective Growth

of 2D Materials: Demonstration of a Bottom-Up CMOS Inverter. *Adv. Mater.* **2019**, *31* (18), 1900861.

(38) Hsu, W.-T.; Zhao, Z.-A.; Li, L.-J.; Chen, C.-H.; Chiu, M.-H.; Chang, P.-S.; Chou, Y.-C.; Chang, W.-H. Second harmonic generation from artificially stacked transition metal dichalcogenide twisted bilayers. *ACS Nano* **2014**, *8* (3), 2951−2958.

(39) He, J.; Hummer, K.; Franchini, C. Stacking effects on the electronic and optical properties of bilayer transition metal dichalcogenidesMoS2, MoSe, WS2. *Phys. Rev. B: Condens. Matter Mater. Phys.* **2014**, *89* (7), No. 075409.

(40) Xia, M.; Li, B.; Yin, K.; Capellini, G.; Niu, G.; Gong, Y.; Zhou, W.; Ajayan, P. M.; Xie, Y.-H. Spectroscopic Signatures of AA′ and AB Stacking of Chemical Vapor Deposited Bilayer MoS2. *ACS Nano* **2015**, *9* (12), 12246−12254.

(41) Pimpinelli, A.; Villain, J. *Physics of Crystal Growth;* Cambridge University Press, 1999. DOI: 10.1017/CBO9780511622526

(42) Oura, K.; Lifshits, V.; Saranin, A.; Zotov, A.; Katayama, M. *Surface Science: An Introduction;* Springer Science & Business Media, 2013.

(43) Aljarb, A.; Fu, J.-H.; Hsu, C.-C.; Chuu, C.-P.; Wan, Y.; Hakami, M.; Naphade, D. R.; Yengel, E.; Lee, C.-J.; Brems, S.; Chen, T.-A.; Li, M.-Y.; Bae, S.-H.; Hsu, W.-T.; Cao, Z.; Albaridy, R.; Lopatin, S.; Chang, W.-H.; Anthopoulos, T. D.; Kim, J.; Li, L.-J.; Tung, V. Ledge-directed epitaxy of continuously self-aligned single-crystalline nanoribbons of transition metal dichalcogenides. *Nat. Mater.* **2020**, *19* (12), 1300−1306.

(44) Unuchek, D.; Ciarrocchi, A.; Avsar, A.; Watanabe, K.; Taniguchi, T.; Kis, A. Room-temperature electrical control of exciton flux in a van der Waals heterostructure. *Nature* **2018**, *560* (7718), 340−344.

(45) Chiu, M. H.; Zhang, C.; Shiu, H. W.; Chuu, C. P.; Chen, C. H.; Chang, C. Y.; Chen, C. H.; Chou, M. Y.; Shih, C. K.; Li, L. J. Determination of band alignment in the single-layer MoS2/WSe2 heterojunction. *Nat. Commun.* **2015**, *6*, 7666.

(46) Kresse, G.; Furthmüller, J. Efficiency of ab-initio total energy calculations for metals and semiconductors using a plane-wave basis set. *Comput. Mater. Sci.* **1996**, *6* (1), 15−50.

(47) Perdew, J. P.; Burke, K.; Ernzerhof, M. Generalized gradient approximation made simple. *Phys. Rev. Lett.* **1996**, *77* (18), 3865.

(48) Klimeš, J.; Bowler, D. R.; Michaelides, A. Van der Waals density functionals applied to solids. *Phys. Rev. B: Condens. Matter Mater. Phys.* **2011**, *83* (19), 195131.